Multiferroic ScLaX_2 (X = P, As, and Sb) monolayers: Bidirectional negative Poisson's ratio effects and phase transformations driven by rare-earth (main-group) elements

Xinyu Tian,[1] Xiao Xie,[1] Jia Li,[1,2] Xiangru Kong,[3] Wei-Jiang Gong,[3] François M. Peeters,[4,5,6] and Linyang Li [1,*]

[1]*School of Science, Hebei University of Technology, Tianjin 300401, China*
[2]*College of Science, Civil Aviation University of China, Tianjin 300300, China*
[3]*College of Sciences, Northeastern University, Shenyang 110819, China*
[4]*Centre for Quantum Metamaterials, HSE University, Moscow 101000, Russia*
[5]*Departamento de Física, Universidade Federal do Ceará, Caixa Postal 6030, 60455–760 Fortaleza, Ceará, Brazil*
[6]*Department of Physics, University of Antwerp, Groenenborgerlaan 171, B-2020 Antwerp, Belgium*

The combination of auxetic property, ferroelasticity, and ferroelectricity in two-dimensional materials offers new avenues for next-generation multifunctional devices. However, two-dimensional materials that simultaneously exhibit those properties are rarely reported. Here, we present a class of two-dimensional Janus-like structures ScLaX_2 (X = P, As, and Sb) with a rectangular lattice based on first-principles calculations. We predict that those ScLaX_2 monolayers are stable semiconductors with both intrinsic in-plane and out-of-plane auxetic properties, showing a bidirectional negative Poisson's ratio effect. The value of the out-of-plane negative Poisson's ratio effect can reach $-2.28/-3.06/-3.89$. By applying uniaxial strain engineering, two transition paths can be found, including the VA main group element path and the rare-earth metal element path, corresponding to the ferroelastic and the multiferroic (ferroelastic and ferroelectric) phase transition, respectively. For the ScLaSb$_2$ monolayer, the external force field can not only control the ferroelastic phase transition, but it can also lead to the reversal of the out-of-plane polarization, exhibiting potential multiferroicity. The coupling between the bidirectional negative Poisson's ratio effect and multiferroicity makes the ScLaX_2 monolayers promising for future device applications.

I. INTRODUCTION

The successful preparation of graphene [1] was the start of a new field of research of atomic thin two-dimensional (2D) materials. Due to the extreme atomic thickness of 2D materials [2], diverse new structures and excellent physical properties, including ferroelectricity, ferroelasticity, and ferromagnetism, can be found. Ferroelectric (FE) materials have tunable spontaneous polarization and can be switched by applying an external electric field, widely used in nonvolatile memory, such as sensors and solar cells [3,4]. Recently, 2D FE materials have been realized experimentally, e.g., In$_2$Se$_3$ [5] and SnSe [6]. Ferroelastic (FA) materials, which exist in two or more stable variants, can be switched by applying an external force field, and they play an important role in shape memory devices [7,8]. Such 2D FA materials have been realized in AgF$_2$ [9] and borophane [10]. Multiferroic materials refer to the simultaneous presence of two or more ferrotypes (ferroelectricity, ferroelasticity, and ferromagnetism) in a material, and the physical coupling between different ferrotypes provides a new avenue for innovative miniaturized electronic storage devices [11,12]. Due to the coupling of ferroelasticity and ferroelectricity, FE phase transition can be achieved by applying an external force field, which provides the possibility for force-controlled polarization reversal [13]. Therefore, the search for multifunctional materials exhibiting FE and FA coupling is our pursuit [14].

At the FA structural phase transition, the change of lattice constant is the basic characteristic leading to the underlying mechanical properties, such as the common positive Poisson's ratio (PPR) effect and the rare negative Poisson's ratio (NPR) effect. Materials with the NPR effect, known as auxetic materials, have attracted much attention due to the unconventional lattice changes under compression or tension [15]. When a transverse tensile strain is applied, the NPR material will expand in the longitudinal direction [16], which was originally realized in three-dimensional (3D) bulk materials [17]. The 2D NPR materials can be divided into two categories, in-plane NPR and out-of-plane NPR. The in-plane NPR materials include penta-graphene [18], silica [19], SiC$_6$ [20] and Be$_2$C [21]. The out-of-plane NPR materials include black phosphorus [22], borophane [10], and BP$_5$ [23]. It was found that there are also bidirectional auxetic materials, which exhibit both in-plane NPR and out-of-plane NPR effects at the same time, such as Ag$_2$S [24], VF$_4$ [25], and GaPS$_4$ [26]. However, such intrinsic bidirectional NPR materials always show relatively small values of NPR, and therefore it is necessary to explore other materials with the NPR effect.

Based on the experiments of successfully synthesized ScN films through methods such as physical vapor deposition [27,28], sputtering [27,29], hydride vapor phase epitaxy, and molecular beam epitaxy (MBE) [30,31], we calculated 12 monolayers composed of the same rare-earth metal (REM)

---

*Contact author: linyang.li@hebut.edu.cn

TABLE I. Lattice constants a, b, a_1, and a_2 (Å); buckling heights h, h_1, and h_2 (Å); polarization values P, P_1, and P_2 (pC/m); and potential barriers E_{b1} and E_{b2} (meV/per cell) of the initial state (IS), the transition state (TS) of the VMG path, and the TS of the REM path.

Monolayer	IS				TS (VMG)				TS (REM)			
	a	b	h	P	a_1	h_1	E_{b1}	P_1	a_2	h_2	E_{b2}	P_2
ScN	4.3	3.8	0.9	0.0	4.2	0.8	290.7	0.0	4.2	0.9	172.4	0.0
ScP	5.0	4.6	1.7	0.0	5.1	0.0	361.4	0.0	4.8	1.7	6.9	−0.1
ScAs	5.1	4.7	2.0	0.0	5.3	0.0	469.7	0.0	4.9	1.9	3.6	0.0
ScSb	5.3	5.0	2.5	0.0	5.7	0.0	601.7	0.0	5.1	2.5	0.6	0.0
YN	4.6	4.0	1.3	0.0	4.4	1.3	127.0	0.0	4.6	0.8	523.8	0.0
YP	5.4	4.7	1.7	0.0	5.4	0.0	319.8	0.0	5.2	1.6	50.3	0.0
YAs	5.6	4.9	1.9	0.0	5.6	0.0	376.5	0.0	5.4	1.8	34.1	0.0
YSb	5.8	5.2	2.4	0.0	6.0	0.0	476.5	0.0	5.6	2.3	14.6	0.0
LaN	4.2	4.6	1.9	0.0	4.4	1.9	12.0	0.0	4.9	0.8	1452.3	0.0
LaP	5.8	4.9	1.6	0.0	5.5	1.5	130.3	0.0	5.7	1.2	305.8	0.0
LaAs	6.0	5.0	1.6	0.0	5.7	1.4	165.7	0.0	5.8	1.3	211.9	0.0
LaSb	6.3	5.2	2.0	0.0	6.2	1.0	217.0	0.0	6.1	1.7	98.3	0.0
ScYN$_2$	4.5	3.8	1.2	8.7	4.2	1.2	179.5	6.5	4.4	0.9	451.6	−0.1
ScYP$_2$	5.3	4.6	1.7	4.7	5.3	0.2	367.5	2.4	5.1	1.6	43.0	0.2
ScYAs$_2$	5.4	4.8	1.9	3.5	5.4	0.0	443.3	−0.4	5.2	1.9	26.9	0.2
ScYSb$_2$	5.6	5.0	2.5	1.6	5.8	0.0	555.2	0.9	5.4	2.5	9.1	0.0
YLaN$_2$	4.1	4.6	1.6	2.8	4.4	1.6	36.7	2.0	4.8	0.8	1171.4	0.0
YLaP$_2$	5.7	4.8	1.5	6.7	5.4	1.1	201.2	10.0	5.5	1.4	213.1	0.0
YLaAs$_2$	5.8	4.9	1.7	6.1	5.6	1.0	244.2	9.6	5.6	1.6	146.0	0.0
YLaSb$_2$	6.1	5.2	2.2	4.2	6.1	0.6	311.8	8.3	5.8	2.1	66.1	0.0
ScLaN$_2$	4.4	3.9	1.5	9.2	4.2	1.6	51.1	6.8	4.6	0.8	1425.8	0.2
ScLaP$_2$	5.5	4.6	1.6	14.4	5.2	1.2	163.0	19.0	5.3	1.5	335.9	0.1
ScLaAs$_2$	5.7	4.7	1.7	12.6	5.4	1.1	203.4	18.0	5.4	1.7	228.6	0.1
ScLaSb$_2$	6.0	5.0	2.2	7.8	5.8	1.0	275.3	16.6	5.7	2.2	94.5	0.0

atoms, and their polarization values are both 0 (Table I). Considering that breaking the inversion symmetry of the structure will introduce spontaneous polarization, we used different REM atoms to break the symmetry along the z-axis forming a Janus-like structure. According to the polarization value and the potential barrier, we selected the ScLaX_2 (X = P, As, and Sb) monolayers for further detailed study. Here, we studied 2D Janus-like structures of ScLaX_2 (X = P, As, and Sb) with a rectangular lattice, which consists of different REM atoms combined with VA main group (VMG) atoms. The symmetry is destroyed by two different REM layers, resulting in the formation of a Janus-like structure. The ScLaX_2 monolayers are stable semiconductors and exhibit a bidirectional NPR effect. The ferroelasticity of the monolayers was investigated by applying strain. For the FA phase transition we found two transition paths, originating from the movement of REM atoms and VMG atoms. We found that the reversal of the polarization direction in the REM path of the ScLaSb$_2$ monolayer can lead to the emergence of ferroelectricity, which should be a multiferroic coupling between FA and FE properties.

II. COMPUTATIONAL METHOD

We perform first-principles calculations in the framework of density functional theory (DFT) using the Vienna *ab initio* Simulation Package (VASP) code [32,33]. Interactions between ions and valence electrons are treated using the projected augmented wave (PAW) method [34,35], and electron exchange correlation functions are treated with Perdew, Burke, and Ernzerhof (PBE) functionals within the generalized gradient approximation (GGA) [36,37]. Atomic positions and planar lattice parameters were fully optimized using a conjugate gradient (CG) scheme until the maximum force on each atom was less than 0.01 eV/Å. In the structure optimization, the energy cutoff point of the plane-wave basis set was set to 500 eV, and the energy accuracy was 10^{-5} eV; a higher energy accuracy of 10^{-7} eV was used in other calculations. The Brillouin zone (BZ) was sampled using a $21 \times 21 \times 1$ centered Monkhorst Pack grid. In all calculations, a vacuum separation of at least 20 Å was employed to minimize all interactions between two neighboring plates. To obtain a more accurate electronic band structure, we also adopted the Heyd-Scuseria-Ernzerhof (HSE06) hybrid function calculation method [38]. Phonon spectra are calculated using the supercell method in the PHONOPY code [39]. The out-of-plane electric dipole moment is obtained through the dipole correction [40], and the transition path and energy barrier of multiferroic materials are obtained by climbing the image nudge elastic band (cNEB) [41].

III. RESULTS AND DISCUSSION

The ScLaX_2 (X = P, As, and Sb) monolayer belongs to the orthorhombic crystal system, and its space group is $Pmm2$. The structures are shown in Figs. 1(a)–1(c), where the black frame represents the unit cell with one Sc atom, one La atom, and two X atoms. The dashed line in the side view represents the position of the REM (Sc/La) atom along the z-axis. From
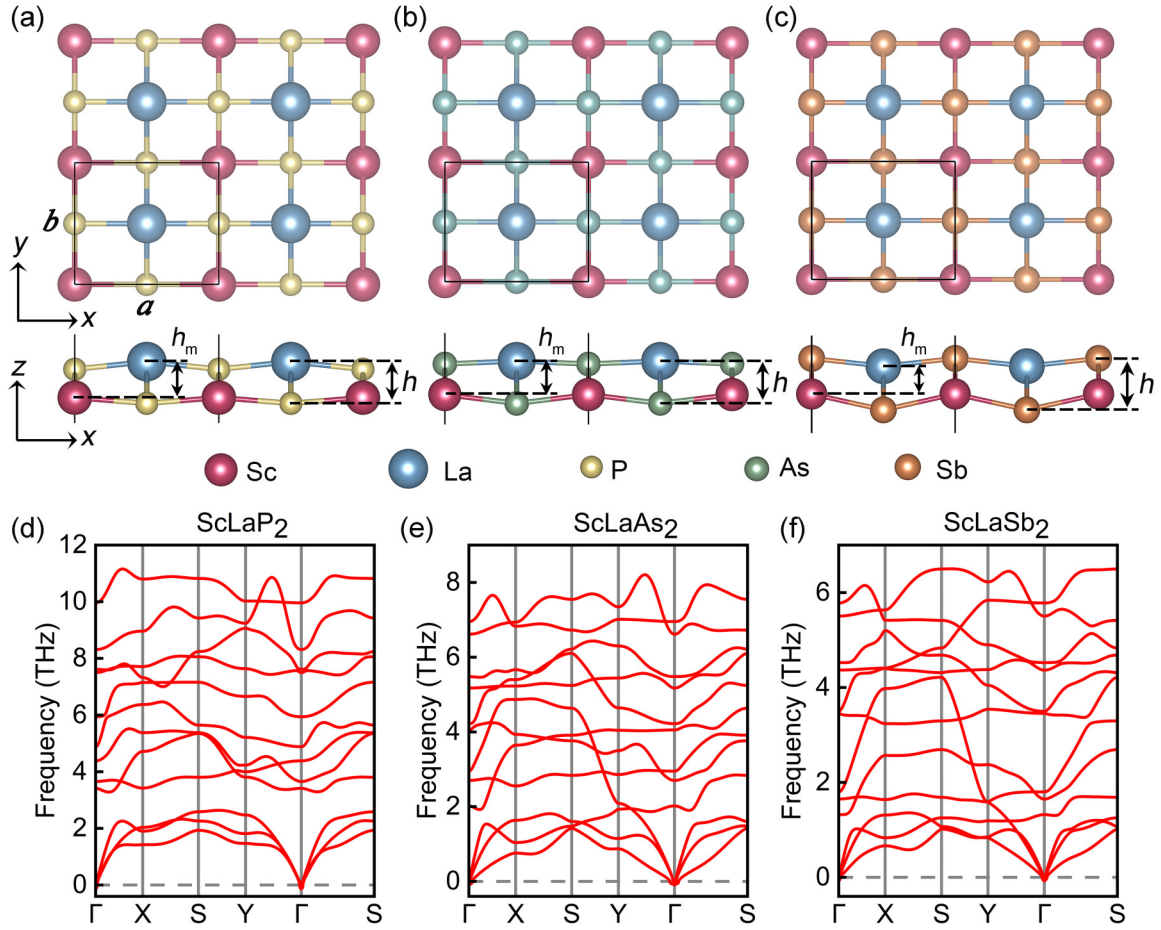
FIG. 1. Optimized structures with top and side views of (a) ScLaP$_2$, (b) ScLaAs$_2$, and (c) ScLaSb$_2$. (d)–(f) Phonon spectra of ScLaX_2 monolayers along the high-symmetry paths.

the side view, P/As atoms partially encapsulate Sc and La atoms along the z-axis in the ScLaP$_2$/ScLaAs$_2$ monolayer [Figs. 1(a) and 1(b)], while Sb atoms completely encapsulate Sc and La atoms in the ScLaSb$_2$ monolayer [Fig. 1(c)]. This phenomenon is similar to the nonmetallic shielding effect [42]. Among the three monolayers, as the relative mass of the VMG elements (P, As, and Sb) increases, their proportion increases in the monolayers, leading to the VMG atoms being closer to the outside. The lattice constants are summarized in Table II. Notice that the lattice constants a, b and the buckling height h of the monolayers become larger with increasing atomic number of the X atom, while at the same time the height difference of REM atoms h_m along the z-axis

TABLE II. Lattice constants a and b (Å), buckling height (thickness) h (Å), height of REM atoms along the z-axis h_m (Å), cohesive energy E_{coh} (eV/atom), Young's modulus (Y_{11} along the x-axis and Y_{22} along the y-axis, N/m), and largest value of in-plane positive/negative Poisson's ratio (PPR/NPR).

ScLaX_2	a	b	h	h_m	E_{coh}	Y_{11}/Y_{22}	PPR/NPR
ScLaP$_2$	5.48	4.63	1.59	1.37	4.64	64.39/13.36	0.476/−0.127
ScLaAs$_2$	5.68	4.72	1.67	1.32	4.33	71.78/11.88	0.335/−0.125
ScLaSb$_2$	6.04	4.97	2.17	1.17	3.88	60.81/8.26	0.253/−0.088

becomes smaller. To further confirm the stability of the monolayers, we calculated the cohesive energy using the following formula [43]: $E_{coh} = (E_{Sc} + E_{La} + 2E_X - E_{ScLaX_2})/4$, where $E_{Sc}/E_{La}/E_X$ are the energy of the isolated Sc/La/X (X = P, As, and Sb) atom, and E_{ScLaX_2} is the total energy of the ScLaX_2 monolayers (per unit cell). The E_{coh} values are summarized in Table II, comparable to silicene (3.98 eV/atom) [44], providing a theoretical basis for the feasibility of experimental synthesis. We calculated the phonon spectrum of these three monolayers, as shown in Figs. 1(d)–1(f); there are no imaginary frequencies indicating their dynamical stability.

Next, we explored the mechanical properties of ScLaX_2 monolayers. The orthorhombic crystal system has four independent elastic constants: C_{11}, C_{12}, C_{22}, and C_{66} [7], as shown in Table S1 in the Supplemental Material [45]. All the values satisfy the condition of mechanical stability ($C_{11}C_{22} - C_{12}^2 > 0$, $C_{66} > 0$) [46]. The in-plane Young's modulus $Y(\theta)$ and Poisson's ratio $\nu(\theta)$ of the ScLaX_2 monolayers were calculated, which can be obtained by the following expressions [47]:

$$Y(\theta) = \frac{C_{11}C_{22} - C_{12}^2}{C_{11}\sin^4\theta + A\sin^2\theta\cos^2\theta + C_{22}\cos^4\theta},$$

$$\nu(\theta) = \frac{C_{12}\sin^4\theta - B\sin^2\theta\cos^2\theta + C_{12}\cos^4\theta}{C_{11}\sin^4\theta + A\sin^2\theta\cos^2\theta + C_{22}\cos^4\theta},$$
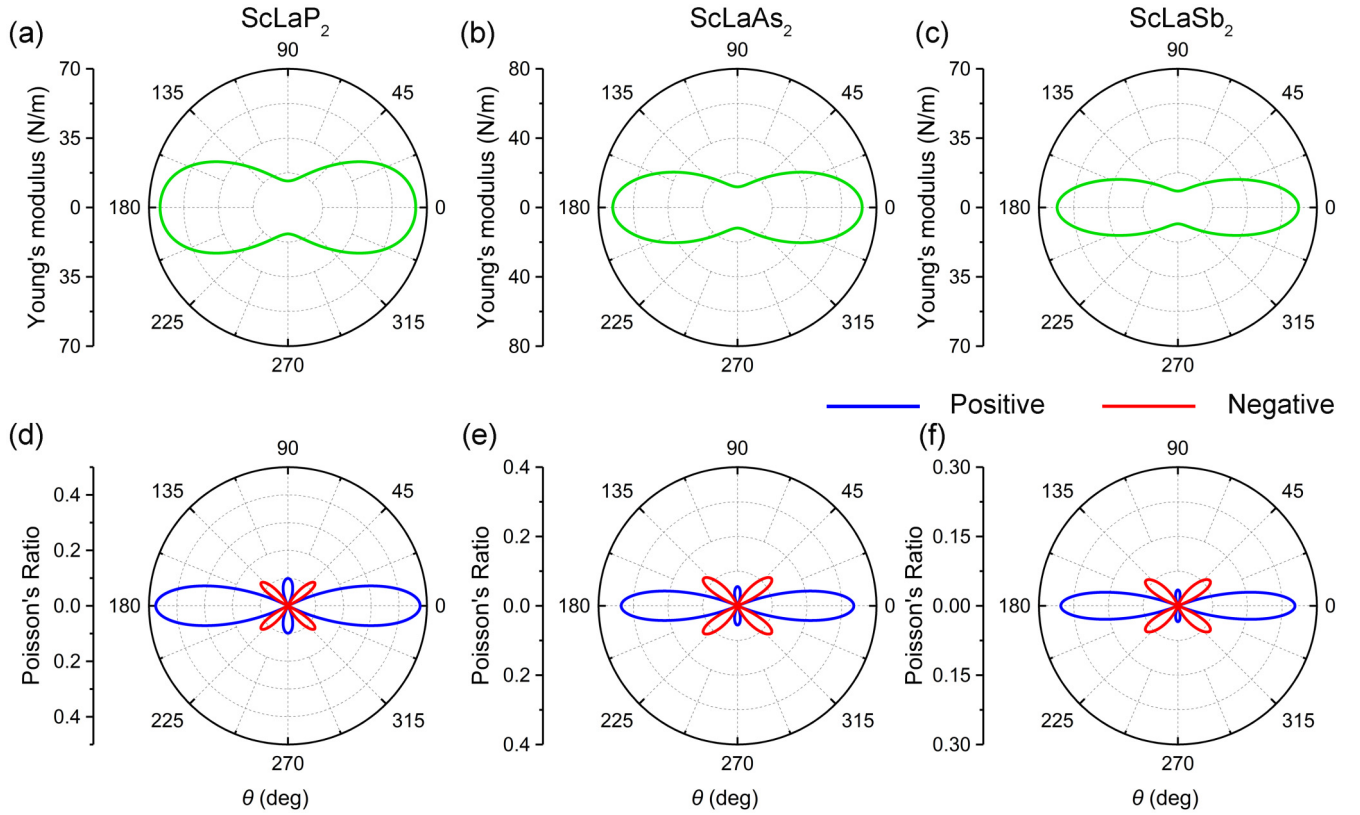
FIG. 2. Young's modulus as a function of angle θ, (a) ScLaP$_2$, (b) ScLaAs$_2$, and (c) ScLaSb$_2$. Poisson's ratios as a function of the angle θ, (d) ScLaP$_2$, (e) ScLaAs$_2$, and (f) ScLaSb$_2$. The blue curves are for PPR and the red curves for NPR.

where $A = (C_{11}C_{22} - C_{12}^2)/C_{66} - 2C_{12}$, $B = C_{11} + C_{22} - (C_{11}C_{22} - C_{12}^2)/C_{66}$, and θ represents the angle with respect to the x-axis. The angle dependence of Young's modulus is shown in Figs. 2(a)–2(c). It can be seen that the maximum values of Young's modulus for the ScLaX_2 monolayers at $0°/180°$ are 64.39/71.78/60.81 N/m, and the minimum values at $90°/270°$ are 13.36/11.88/8.26 N/m, reflecting the anisotropy. Those values are significantly smaller than that of graphene (340 N/m) [48]/h-BN (275.8 N/m) [49], indicating that the monolayers are soft. The anisotropy can be described by the ratios of Y_{11}/Y_{22}, which are 4.82/6.04/7.36 for the ScLaX_2 monolayers, respectively. With increasing atomic number of VMG elements, the anisotropy increases. The in-plane Poisson's ratios are shown in Figs. 2(d)–2(f). All exhibit a similar butterfly-shaped in-plane Poisson's ratio with the presence of NPR. The angle of the maximum in-plane NPR of the ScLaP$_2$/ScLaAs$_2$/ScLaSb$_2$ monolayer is $41°/39°/38°$, with the corresponding NPR value of $-0.127/-0.125/-0.088$. These values are larger than that of tetra-silicene (-0.055)/PN (-0.078) [50,51], and comparable to that of Ag$_2$S (-0.12)/Be$_5$C$_2$ (-0.16) [24,52], which originates from the anisotropy of the ScLaX_2 monolayers.

Here, we started from the structure of ScLaSb$_2$ monolayer to explore the origin of in-plane NPR. Figure S1 shows the tetrahedral pucker structure formed by REM atoms (Sc and La) and four neighboring Sb atoms. To understand the chemical bonds, the electron localization function (ELF) diagrams along the (010) and (100) surfaces are shown in Fig. S2. It is obvious that the electrons are located around

the atoms, and there is almost no electron density between Sc atoms and neighboring P/As/Sb atoms, indicating typical ionic bonds. However, there is delocalized electron density between La atoms and neighboring P/As/Sb atoms, indicating the presence of covalent bonds [53]. The ionic bonds have no directional preference, leading to nontrivial mechanical responses. When external strain is applied along the x-axis or y-axis, the contraction/expansion of the tetrahedral volume will lead to PPR. When tensile strain is applied along the α direction, the tetrahedron rotation will be easier than in other directions, in which the tetrahedrons A and C (B and D) will rotate clockwise (counterclockwise) (Fig. S1). This will lead to expansion in the β direction, exhibiting the NPR effect [54]. At $41°/39°/38°$ near the diagonal direction of the ScLaX_2 monolayer, the rotation of the tetrahedron is the greatest, leading to the maximum value of NPR.

Here, to gain a deeper understanding of the NPR effect in ScLaX_2 monolayers, we calculated their phonon density of states (DOS) to reveal potential structural influences (Fig. S3). First, the NPR effect depends on the crystal structure, and ScLaX_2 monolayers with similar structures exhibit NPR effects. In this paper, we provided a structural explanation for the NPR mechanism, where the emergence of in-plane NPR is related to the tetrahedral pucker structure (Fig. S1). Second, the phonon DOS reflects the distribution of different types of phonon vibration modes in the material, which is of great significance for understanding the mechanical behavior of the material, and therefore we will conduct a detailed analysis of the vibration modes of ScLaX_2 monolayers. As

shown in Fig. S3(a), in the low-frequency region (0–2 THz) of the ScLaP$_2$ monolayer, La atoms exhibit significant peaks. The low-frequency region of the phonon DOS is usually related to long-range vibrations of the lattice and overall structural deformation. This indicates that La atoms exhibit more pronounced vibration during overall deformation. In the midfrequency region, it usually involves local structural rearrangements of smaller scale or relative atomic motion. At 2–8 THz, the small-scale relative motion between Sc and P atoms is more pronounced. In the high-frequency region, corresponding to 8–12 THz, P atoms exhibit sharp peaks, indicating strong interactions with surrounding atoms. The analysis shows that due to the strong interactions between P atoms and surrounding atoms, applying external strain to the ScLaP$_2$ monolayer leads to a preference for structural rotation in specific directions rather than volume change, and the relative motion between Sc and P atoms leads to abnormal structural responses. In the ScLaAs$_2$ monolayer, as shown in Fig. S3(b), we mainly focus on the midfrequency region (2–6 THz), where the As (3 THz) and Sc (4 THz) atoms exhibit sharp peaks, indicating that the local vibrational modes of the atoms are more pronounced. In the high-frequency range (6–8 THz), the sharp peaks of the As and Sc atoms indicate strong interactions. The special vibrational modes between As and Sc atoms are important to the NPR behavior. For the midfrequency region (1–4 THz) of the ScLaSb$_2$ monolayer, as shown in Fig. S3(c), the Sb atoms exhibit significantly concentrated peaks, indicating that the vibration of Sb atoms is the main reason for the NPR effect. For the emergence of the NPR effect in the ScLaX_2 monolayers, we mainly attribute it to the pronounced vibrations of X atoms and the strong interactions between X atoms and surrounding atoms. This result leads to easier rotation of tetrahedral pucker structure when external strain is applied in specific directions (Fig. S1), leading to an unconventional structural response.

Furthermore, the variation of phonon frequency range in the phonon DOS is directly related to the elastic modulus and structure. In the phonon DOS diagram, it can be found that as the atomic number of X (P, As, and Sb) atoms increases, the frequency range of the main contribution of X atoms gradually decreases, shifting from the optical branch to the acoustic branch. With the phonon vibration mode more localized, the highest cutoff frequency gradually decreases (11.20/8.22/6.53 THz). From the perspective of elastic modulus, low phonon frequencies correspond to low stiffness materials. As the frequency gradually decreases, it can be preliminarily reflected that the elastic modulus of the material gradually decreases [55]. The peak intensity in the phonon DOS usually corresponds to harder bonding or higher elastic modulus. The abnormal changes observed in C_{11} of ScLaAs$_2$ can be attributed to the sharp peak of the Sc atom at 4 THz. From the perspective of structure, in similar structures the low-frequency modes of phonons have longer wavelengths, corresponding to larger crystal structures [56]. As the electronegativity difference between Sc/La and X atoms decreases, the bond strength of heavier X atoms weakens [57]. Therefore, applying external strain along the α direction weakens the response along the β direction, thereby weakening the in-plane NPR effect ($-0.127/-0.125/-0.088$). Overall, through the analysis of vibration modes in the phonon

DOS, we gained a deeper understanding of the special vibration modes that trigger the NPR effect in ScLaX_2 monolayers. By analyzing the phonon DOS, we elucidated the complex relationship between structural characteristics, vibration mode, and the NPR effect.

The electronic band structures of ScLaX_2 monolayers are shown in Fig. 3. We calculated the PBE electronic band structure of ScLaX_2 monolayers and found that they are all indirect band gap semiconductors. For the ScLaP$_2$/ScLaAs$_2$ monolayer, the valence-band maximum (VBM) is located at the Γ point while the conduction-band minimum (CBM) is located along the path YΓ, and the band gap is 0.52/0.58 eV. For the ScLaSb$_2$ monolayer, the VBM (CBM) is located at the Y point (along the path YΓ), and the band gap is 0.64 eV. We also searched for 12 experimentally synthesized bulk materials AB ($A =$ Sc, Y, La and $B =$ N, P, As, Sb) with face-centered-cubic (fcc) cell structures. By slicing on the (110) plane of the fcc structure, a 2D structure similar to the predicted material in this paper can be obtained [58], and the 2D structural information of the 12 materials is summarized in Table I. We only found the band gap of the bulk ScN and LaN that were measured in the experiment. Therefore, in Fig. S4, we used the HSE06 hybrid functional method to calculate the electronic band structures of bulk ScN and LaN. We compared these results with experimental results to verify the accuracy of the HSE06 method in predicting electronic band structures. The calculated indirect band gap (Γ to X) of ScN is 0.92 eV, while the experimental values range from 0.8 to 1.0 eV, which are close to each other [29,59,60]. Similarly, for LaN, we calculated a direct band gap of 0.83 eV at the X point, while the experimental value is 0.82 eV, showing only a difference of 0.01 eV [61]. The above results provide a reliable basis for the HSE06 functional in predicting the electronic properties of REM-VMG systems. Therefore, for further electronic band structure calibration, we also used the calculation method of the HSE06 functional. At the HSE06 level, the band-gap value of ScLaX_2 monolayers is increased to 0.99/1.08/1.18 eV. As shown in Fig. 3, near the Fermi level, the calculated PBE electronic band structure shows a similar trend to HSE06, proving the reliability of the PBE calculation method. Next, we considered the PBE band structure with the spin-orbit coupling (SOC) effect. As shown in Fig. S5, a slight band splitting due to the Rashba effect can be observed. The band-gap values become 0.51/0.57/0.56 eV, respectively, which are close to the value without SOC. The projected band structures of ScLaX_2 monolayers are shown in Figs. S6–S8. Here, the X atoms have the largest total contribution to the VBM, and the Sc atom has the largest total contribution to the CBM. We investigated further the contributions of the individual orbitals of the atoms. Obviously, the p_x orbital of the X atom plays an important role for the VBM, while the d_{xy} and d_{xz} orbitals of the Sc atom make the main contributions to the CBM.

Since the structural properties of ScLaP$_2$ and ScLaAs$_2$ monolayers are almost the same, we will only focus on ScLaP$_2$ and ScLaSb$_2$ monolayers in the following discussion. For 2D materials, it is generally easier to apply tensile strain than compressive strain [62], and therefore we applied uniaxial strain to ScLaP$_2$ and ScLaSb$_2$ [63]. The uniaxial strain along the y-axis was applied, and the response of each
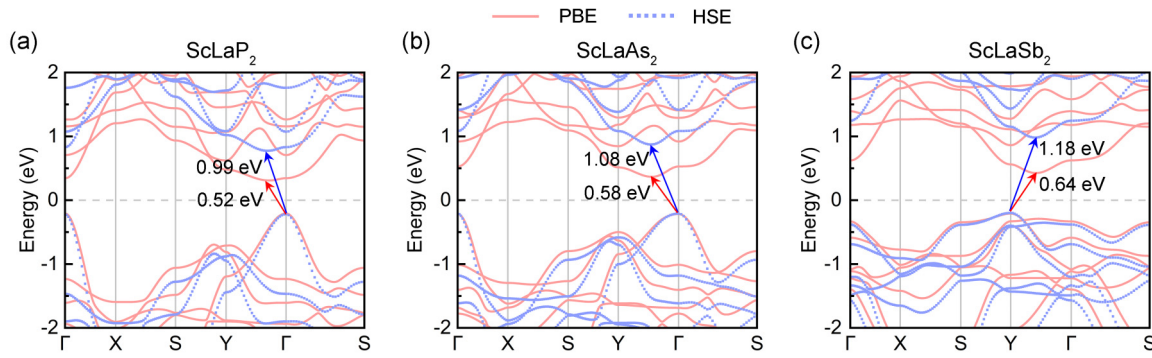
FIG. 3. Band structures of (a) $ScLaP_2$, (b) $ScLaAs_2$, and (c) $ScLaSb_2$. The pink solid curves represent the band structure from PBE, and the blue dotted curves represent the band structure from HSE06.

property is shown in Fig. 4. For clarity, the strain is defined as $\varepsilon = (l - l_0)/l_0$, where $\varepsilon = \varepsilon_x$, ε_y, and ε_z correspond to the strain response along the x-, y-, and z-axis, respectively. Here, $l = a$, b, and h ($l_0 = a_0$, b_0, and h_0) denote the lattice parameters along the x- and y-axis and the buckling height under strain (without strain), respectively. With the uniaxial strain along the y-axis, ε_x shows a decreasing trend, which is a common for the PPR effect [Figs. 4(a) and 4(e)]. There are three special structural phases with lattice constants (a and b), including the initial state (IS) of $a > b$, the transition state (TS) of $a = b$, and the final state (FS) of $a < b$, which should be a FA phase-transition process. Under external strain, FA can generate at least two oriented variants, which are structurally equivalent with equal stability [7,63]. We applied -5% to 25% uniaxial strain to investigate the complete FA transition process of $ScLaX_2$ monolayers, which is a reasonable strain range. The large strain range is due to the structural phase transition occurring during the FA transition process. In previous works, the strain range for t-VP reached 23.4% [64], AgO monolayer reached 24% [65], and borophane reached as high as 42% [10]. Xuan *et al.* [66] used a large strain range ($-25.1\% \sim 20.5\%$) in their study of the FeAsF monolayer. It is worth noting that Zhang *et al.* [67] applied a huge strain range of up to 73% when studying the FA phase transition of the Janus VSSe monolayer. The FS structure of FA phase for the $ScLaP_2$/$ScLaSb_2$ monolayer can be obtained under strain of about 18%/22% [Figs. 4(b) and 4(f)]. Here, the 25% strain is relative to the IS, but for the FS it is only equivalent to applying strain of 7%/3%. For a stable 2D structure, the strain of 7%/3% is reasonable. Subsequently, we confirmed the dynamical stability of the FS structure of the $ScLaP_2$/$ScLaSb_2$ monolayer by the phonon spectrum, as shown in Figs. S9(a)/S9(b). Taking the $ScLaSb_2$ monolayer as an example, we confirmed the dynamical stability under strain of up to 25% and found a slight imaginary frequency near the Γ point [Fig. S9(c)]. This is due to size and boundary effects, which are expected to disappear in relatively large supercells [68]. Furthermore, its thermal stability by conducting *ab initio* molecular dynamics (AIMD) simulations at 300 K for 10 ps was confirmed [Fig. S9(d)]. The potential energy exhibits fluctuations around a stable value, and no structural deformation or bond breaking occurs upon completion, indicating satisfactory thermal stability. The FA phase-transition process is governed by a double potential well [Figs. 4(b) and 4(f)],

with a potential barrier of 0.16/0.09 eV per unit cell. During the uniaxial strain along the y-axis, the two monolayers exhibit semiconductor properties, and the value of the band gap decreases at first and then increases [Figs. 4(c) and 4(g)]. Note that uniaxial strain can drive the transition between a direct and an indirect semiconductor. The $ScLaP_2$ and $ScLaSb_2$ monolayers show similar results for this structure, energy, and band structure during the phase transitions. However, the phase transition of polarization along the z-axis is different. The polarization values of the $ScLaP_2$ monolayer show a peak shape with positive values [Fig. 4(d)], which are 14.5 pC/m at the IS/FS, and 19.0 pC/m at the TS. However, the polarization values of $ScLaSb_2$ monolayer shows a reversal process, where it is 7.6 pC/m (-7.8 pC/m) at the IS (FS), and it is zero at the TS, exhibiting a FE phase transition. For FE materials, each ground-state structure has two equivalent states with opposite polarizations, which are energy degeneracy and equally stable [69]. The dynamical stability of the negative polarization (FS) of the $ScLaSb_2$ monolayer was confirmed by its phonon spectrum [Fig. S9(b)], where no imaginary frequency was found.

To further explain the different results for the polarization values, we studied the atomic positions along the z-axis for the $ScLaP_2$ and $ScLaSb_2$ monolayers. Due to this Janus-like structure, there can be a redistribution of charges [70,71], and the significant height difference and electronegativity disparity between the two REM atoms (Sc and La) should result in out-of-plane polarization. The direction of polarization goes from negative charge to positive charge. In such a monolayer, it should be from Sc atoms towards La atoms along the z-axis. For the $ScLaP_2$ monolayer, the polarization values are all positive [Fig. 4(d)]. This can be explained from the atomic displacements [Fig. 4(i)], in that only the P_1 and P_2 atoms exchange their positions along the z-axis, and the relative positions of REM atoms remain unchanged, leading to the same polarization direction from Sc to La. However, it is different for the $ScLaSb_2$ monolayer. The polarization values are opposite in the IS and FS, and the value is zero in the TS. From the atomic displacements along the z-axis [Fig. 4(m)], the positions of REM atoms are exchanged, resulting in a reversal of the polarization direction in the IS and FS. In the TS, the REM atoms move to the same xy-plane with the same position along the z-axis, leading to a zero polarization value. Based on the above results, it is obvious that the $ScLaP_2$ and $ScLaSb_2$ monolayers exhibit two FA phase-transition paths.
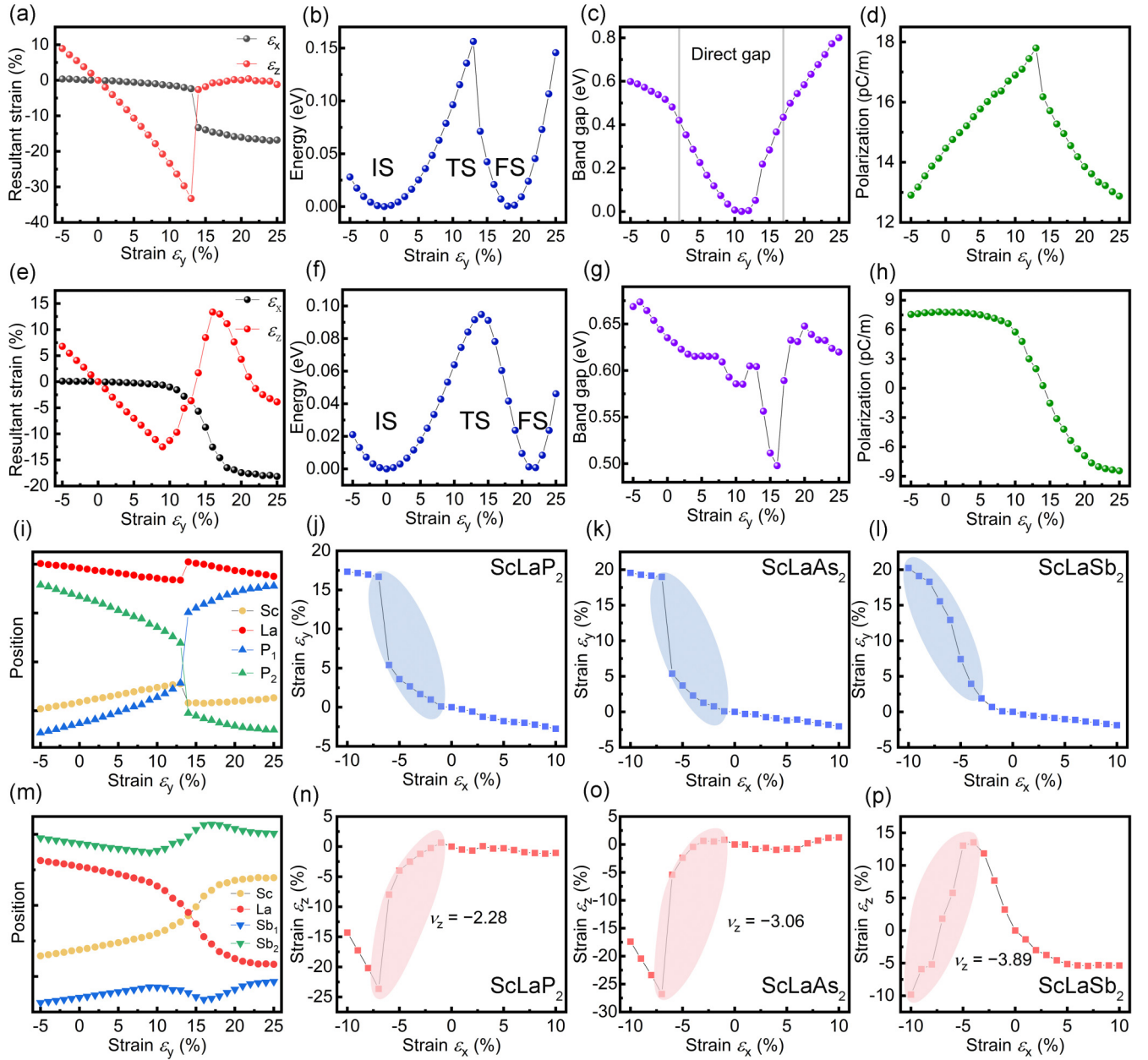
FIG. 4. Uniaxial strain is applied to the ScLaP$_2$/ScLaSb$_2$ monolayer along the y-axis. (a)/(e) is the strain responses along the x-axis/z-axis. (b)/(f) is the variation of total energy. (c)/(g) is the variation of band gap. (d)/(h) is the variation of polarization value. (i)/(m) is the atomic position variation along the z-axis. Uniaxial strain is applied along the x-axis of the ScLaX_2 monolayer. (j)–(l) Strain response along the y-axis, and (n)–(p) strain response along z-axis.

We named the path from the exchange of VMG atoms (P$_1$ and P$_2$) in the ScLaP$_2$ monolayer as the VMG element path. In the ScLaSb$_2$ monolayer, we named the path from the exchange of REM atoms (Sc and La) as the REM element path. For the monolayers of ScN [72], FeAs [66], InBi [73], CuTe [74], VX (X = P, As) [75], VP [64], TiSe [76], and YbX (X = S, Se, Te) [54], all are rectangular lattice structures with ferroelasticity. The FA phase transition is triggered by the exchange of metal atoms along the z-axis, corresponding to the REM element paths proposed in our study. To the best of our knowledge, the VMG element path provides a new perspective for the FA phase transition of rectangular lattice structures. In

Table I, we also calculated the potential barriers of other monolayers by the two transition paths. Among them, The VMG path barrier of YN, LaN, LaP, LaAs, ScYN$_2$, YLaN$_2$, YLaP$_2$, ScLaN$_2$, ScLaP$_2$, and ScLaAs$_2$ monolayers is lower, and these monolayers will choose the VMG path. We found that the choice of path is determined by the structure. If the VMG element completely surrounds the REM element in the side view, the REM element path will be selected, otherwise the VMG element path will be selected.

To further confirm the VMG and REM paths, we calculated the transition states of ScLaX_2 monolayer by the two paths [Figs. 5(a) and 5(b)]. The path passes through TS from IS to
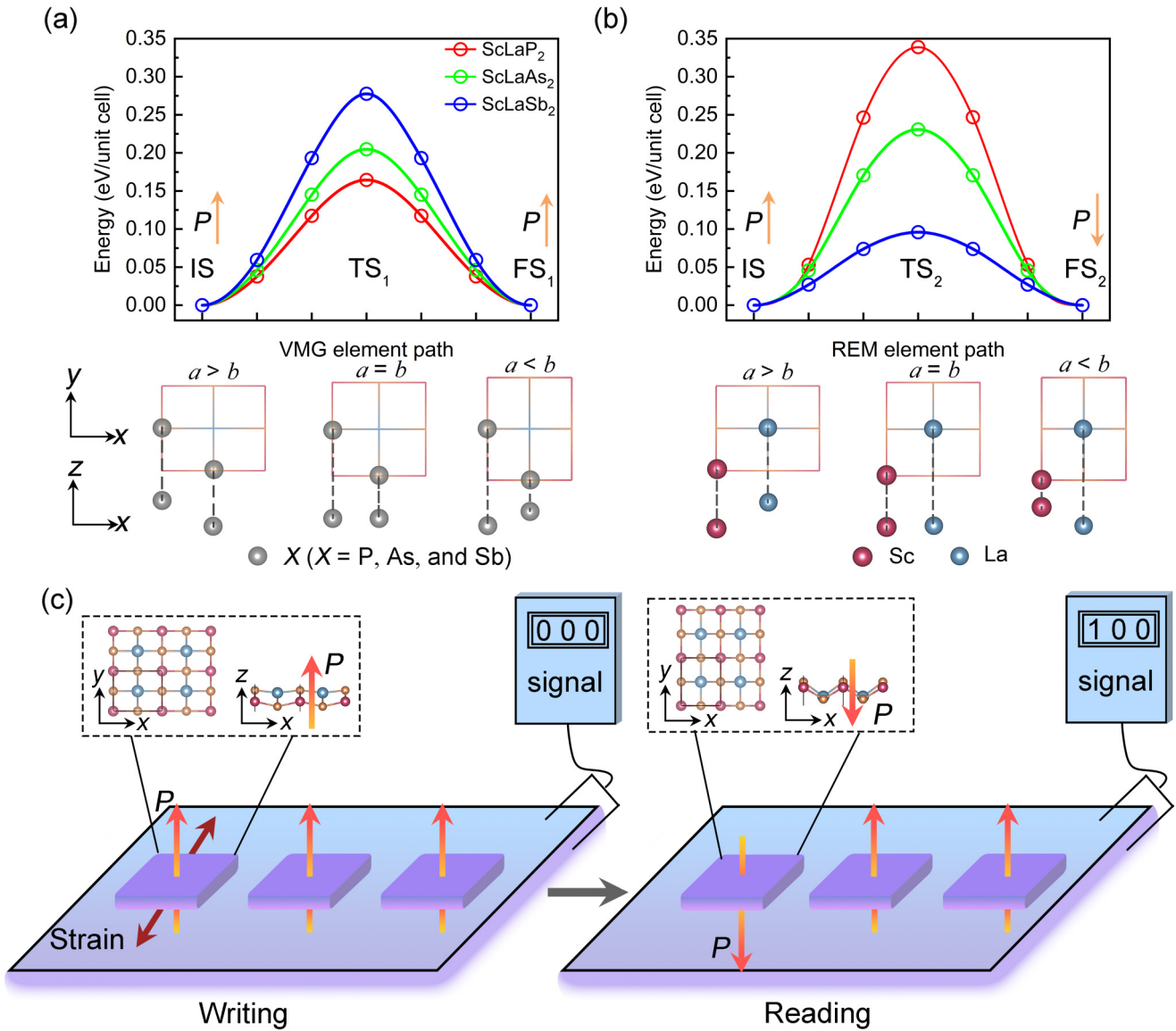
FIG. 5. Energy distribution of ScLaX_2 monolayers of (a) VMG element path and (b) REM element path. The diagram below illustrates a simplified structure and represents the positional changes of atoms along the z-axis in the FA phase transition. (c) Nonvolatile electronic memory device model, where the red (orange) arrows represent the directions of applied external strain (spontaneous polarization). The illustration takes ScLaSb$_2$ monolayer as an example.

FS, showing a double-well shape. For the VMG element path, the potential barrier is 162.46/202.86/275.19 meV per unit cell for ScLaP$_2$/ScLaAs$_2$/ScLaSb$_2$, which should be a FA phase transition. For the REM element path, the potential barrier becomes 335.78/228.85/94.83 meV per unit cell, where the lattice constant and polarization direction are reversed at the same time, which should be a FA and FE phase transition. The coupling of FA and FE occurs in the REM element path, which realizes the transition of force/electric-field-controlled crystal structure, and the moderate switching barrier ensures the experimental possibility of FA and FE phase transitions. When strain is applied to the ScLaX_2 monolayer, it should go through the path with the lowest potential barrier. The ScLaP$_2$ and ScLaAs$_2$ monolayers prefer the VMG element path, while the ScLaSb$_2$ monolayer prefers the REM element path. Therefore, there is a coupling effect of FA and FE for

the REM element path of the ScLaSb$_2$ monolayer. When a force field is applied to a ScLaSb$_2$ monolayer, it will lead to changes of the crystal lattice [13] and the redistribution of charges. To observe the strain effect on the charge distribution for the ScLaSb$_2$ monolayer, we used Bader charge analysis to show the charge-transfer changes in IS, TS, and FS. Figure S10 clearly shows the changes of charge transfer with strain. Negative values indicate the loss of electrons, while positive values indicate the acquisition of electrons. It can be found that electrons are transferred to the Sb atoms from the REM atoms (Sc and La). At IS/FS, the charges transferred from the REM atoms to the Sb$_1$ atoms are about 1.43/1.48 electrons, while the charges transferred to the Sb$_2$ atoms are about 1.48/1.43 electrons, showing an opposite trend. At TS, about 1.48 electrons are transferred equally from the REM atoms to Sb$_1$ and Sb$_2$ atoms. Therefore, applying

external forces can trigger a series of chain interactions of force field–lattice–charge polarization, leading to the reversal of force-field-controlled polarization and truly forming a coupling mechanism between the force field and the multiferroic.

The structures of the IS, TS, and FS in the VMG and REM paths are shown in Fig. S11. For the IS state, the two paths exhibit the same structure. For TS_1/TS_2, the VMG/REM atoms are on the same plane, while IS and FS_1/FS_2 are essentially the same and can achieve FA switch-controlled structural anisotropy output [77]. We also calculated the corresponding band structure of each state (Fig. S12). Only the TS_1 of ScLaSb$_2$ in the VMG element path shows a metallic property, while all the other states are indirect band gap semiconductors, where the band-gap values are $0.14-0.64$ eV. In addition, the out-of-plane polarization values for each state were calculated and summarized in Tables S2 and S3. The potential difference diagrams generated by the nonoverlapping positive and negative charge centers are shown in Figs. S13–S15, further confirming the correctness of the calculation of the polarization values. An interesting phenomenon can be found from Tables S2 and S3, where the h_m of TS_1 is smaller than that of IS/FS_1 in the VMG element path, but its polarization value is larger. This is because the VMG atoms have a tendency to structurally encapsulate the REM atoms, acting as a "protective barrier" (nonmetallic shielding performance) [42], and the VMG atoms have a larger electronegativity than the REM atoms. When reaching TS_1, the VMG atoms are in a plane and surrounded by REM atoms, and the "shielding" effect disappears, resulting in an increase in the polarization value.

An important criterion for the relevance of the FA performance of ScLaX_2 monolayer is reversible strain, which is defined as $(|a|/|b| - 1) \times 100\%$ [58]. The reversible strain of ScLaX_2 is 18.37%/20.31%/21.52%, which is higher than SnS (4.9%) and SnSe (2.1%) [78]. The higher the reversible strain, the stronger the signal displayed by the FA phase transition. We obtained the spontaneous lattice strain matrix η of the two paths by using the Green-Lagrange strain tensor theory [8], calculated by the following formula: $\eta = \frac{1}{2}[(H_0^{-1})^T H_i^T H_i H_0^{-1} - I]$, where H_0 (H_i) represents the TS (FA) phase, and I represent the identity matrix. η is the strain matrix of the 2D transformation: $\eta = \begin{pmatrix} \varepsilon_{xx} & \varepsilon_{xy} \\ \varepsilon_{xy} & \varepsilon_{yy} \end{pmatrix}$, where ε_{xx}, ε_{yy}, and ε_{xy} serve as elements of the 2D transformed strain tensor, representing the axial strain along the x-axis, the y-axis, and shear strain, respectively [79]. The formula can be simplified as [80]

$$\eta = \begin{pmatrix} (\frac{a^2}{c^2} - 1)/2 & 0 \\ 0 & (\frac{b^2}{c^2} - 1)/2 \end{pmatrix},$$

where a, b (c) are the lattice constants of the FA (TS) phase. We calculated the spontaneous lattice strain matrices, as shown in Tables S2 and S3. Taking ScLaP$_2$ in the REM element path (Table S3) as an example, its strain matrix is $[0.033, 0; 0, -0.120]$, showing that the tensile strain along the x-axis is 3.3% and the compressive strain along the y-axis is 12%. This significant strain response allows the system to respond quickly to an external force field.

Due to the novel properties exhibited by the ScLaX_2 monolayer, we show its potential application in nanoelec-

tronic devices [78] and we propose a model for a nonvolatile memory device [Fig. 5(c)]. The memory device model consists of electric writing and reading components. Device information is represented in binary form. In the left illustration, the writing device can encode information as "0 0 0" [23]. By applying external strain, the material undergoes a FA phase transition, triggering spontaneous polarization direction switching. Ultimately, the information "1 0 0" is preserved in the reading device, achieving permanent memory in the form of nonvolatile memory. Information reading can be accomplished by measuring the potential difference on the device, where the potential difference can reflect the stored information, enabling the retrieval of encoded data. This device realizes polarization reversal controlled by an external force field, providing electronic storage devices with more flexible and controllable means of operation.

From the uniaxial strain along the y-axis, the ε_z has an upward trend, showing an out-of-plane NPR effect [Figs. 4(a) and 4(e)]. To further confirm this, we applied a uniaxial strain range of $\pm 10\%$ for the x-axis, and the strain response of ε_y is shown in Figs. 4(j)–4(l), showing a gradually decreasing trend, exhibiting the PPR effect. The ε_z is shown in Figs. 4(n)–4(p), showing an upward trend, indicating the appearance of the out-of-plane NPR effect. The value of out-of-plane NPR can be obtained by fitting $y = -\nu_1 x + \nu_2 x^2 + \nu_3 x^3$, where x (y) is the applied strain (strain response), and ν_1 is the value of Poisson's ratio [65]. The out-of-plane NPR strain range of ScLaP$_2$ (ScLaAs$_2$) is -7% to -1%, and the fitted value is -2.28 (-3.06). The strain range of ScLaSb$_2$ is -10% to -4%, and the NPR value is -3.89. The origin of out-of-plane NPR can be explained by the geometric response of its structure when uniaxial strain is applied. Taking the ScLaSb$_2$ monolayer as an example [Fig. S16(a)], the triangles formed by Sc$-$Sb$_2-$Sc and Sb$_1-$La$-$Sb$_1$ constitute the shaded regions with heights h_1 and h_2. Set $L = h_1 + h_2 = \sqrt{L_1^2 - \frac{b^2}{4}} + \sqrt{L_2^2 - \frac{b^2}{4}}$, where L_1 and L_2 represent the distances between Sc$-$Sb$_2$ and La$-$Sb$_1$, and b represents the lattice constant along the y-axis. The total thickness of the structure can be expressed as $H = L - h_m = \sqrt{L_1^2 - \frac{b^2}{4}} + \sqrt{L_2^2 - \frac{b^2}{4}} - h_m$, where $h_m = h_{La} - h_{Sc}$ represents the height difference between the two REM atoms. In the process of applying external strain, the FA phase transition occurs, where L can characterize the in-plane FA phase mechanism due to the change of b, while h_m represents the out-of-plane FA phase transition mechanism. Therefore, the H can be understood as the competitive mechanism between in-plane (L) and out-of-plane (h_m) FA phase transitions. We show the curves of the variations in L and h_m with uniaxial strain ε_x [Fig. S16(b)]. Observably, during the out-of-plane NPR (-4% to -10%) close to the TS state of the FA phase transition [blue area of Fig. 4(l)], the decrease of L is faster than that of h_m, introducing a decrease of H. Therefore, when external strain ε_x is applied (from -4% to -10%), the total thickness H of the monolayer exhibits an abnormal decreasing trend, leading to the emergence of the out-of-plane NPR effect, which should be attributed to the competitive mechanism between in-plane and out-of-plane structural changes in the FA phase transition.

IV. CONCLUSION

In summary, we predict a new class of 2D Janus-like structures ScLaX_2 (X = P, As, and Sb) by DFT, exhibiting bidirectional NPR and multiferroicity. For the NPR effect of the ScLaX_2 monolayers, the value of the in-plane NPR is $-0.127/-0.125/-0.088$ and the value of the out-of-plane NPR is $-2.28/-3.06/-3.89$. The bidirectional NPR effect originates from the in-plane anisotropy and the FA phase transition. For the multiferroicity of the ScLaX_2 monolayers, the VMG element path corresponds to the FA phase transition while the REM element path corresponds to the FA and FE phase transition. By applying strain engineering, the coupling in the FA and FE phase transition can be found in the ScLaSb$_2$ monolayer. Furthermore, the coupling of FA, FE, and NPR can be used in nonvolatile memory, and the structural phase transition leading to the change of the physical property can be controlled by an applied force field. The ScLaX_2 monolayers have both bidirectional NPR and multiferroic properties, providing more development space for future device applications.

[1] K. S. Novoselov, A. K. Geim, S. V. Morozov, D. Jiang, Y. Zhang, S. V. Dubonos, I. V. Grigorieva, and A. A. Firsov, Science **306**, 666 (2004).

[2] S. Z. Butler, S. M. Hollen, L. Cao, Y. Cui, J. A. Gupta, H. R. Gutiérrez, T. F. Heinz, S. S. Hong, J. Huang, A. F. Ismach, E. Johnston-Halperin, M. Kuno, V. V. Plashnitsa, R. D. Robinson, R. S. Ruoff, S. Salahuddin, J. Shan, L. Shi, M. G. Spencer, M. Terrones, W. Windl, and J. E. Goldberger, ACS Nano **7**, 2898 (2013).

[3] M. Wu, S. Dong, K. Yao, J. Liu, and X. C. Zeng, Nano Lett. **16**, 7309 (2016).

[4] Z.-X. Shen, X. Ren, and L. He, Appl. Phys. Lett. **112**, 103901 (2018).

[5] X. Tao and Y. Gu, Nano Lett. **13**, 3501 (2013).

[6] K. Chang, F. Küster, B. J. Miller, J.-R. Ji, J.-L. Zhang, P. Sessi, S. Barraza-Lopez, and S. S. P. Parkin, Nano Lett. **20**, 6590 (2020).

[7] T. Zhang, Y. Ma, L. Yu, B. Huang, and Y. Dai, Mater. Horiz. **6**, 1930 (2019).

[8] W. Li and J. Li, Nat. Commun. **7**, 10843 (2016).

[9] X. Xu, Y. Ma, T. Zhang, C. Lei, B. Huang, and Y. Dai, Nanoscale Horiz. **5**, 1386 (2020).

[10] L. Kou, Y. Ma, C. Tang, Z. Sun, A. Du, and C. Chen, Nano Lett. **16**, 7910 (2016).

[11] M. Wu and P. Jena, Wiley Interdiscip. Rev.: Comput. Mol. Sci. **8**, e1365 (2018).

[12] X. Tang and L. Kou, J. Phys. Chem. Lett. **10**, 6634 (2019).

[13] H. Lu, C.-W. Bark, D. Esque de los Ojos, J. Alcala, C. B. Eom, G. Catalan, and A. Gruverman, Science **336**, 59 (2012).

[14] K.-R. Hao, X.-Y. Ma, H.-Y. Lyu, Z.-G. Zhu, Q.-B. Yan, and G. Su, Nano Res. **14**, 4732 (2021).

[15] S. Xu, X. Ma, Y. Li, Y. Qu, and M. Zhao, ACS Appl. Electron. Mater. **4**, 2264 (2022).

[16] R. Lakes, Science **235**, 1038 (1987).

[17] J. Dagdelen, J. Montoya, M. De Jong, and K. Persson, Nat. Commun. **8**, 323 (2017).

[18] S. Zhang, J. Zhou, Q. Wang, X. Chen, Y. Kawazoe, and P. Jena, Proc. Natl. Acad. Sci. USA **112**, 2372 (2015).

[19] Z. Gao, X. Dong, N. Li, and J. Ren, Nano Lett. **17**, 772 (2017).

[20] X. Liu, X. Shao, B. Yang, and M. Zhao, Nanoscale **10**, 2108 (2018).

[21] S. Qian, X. Sheng, Y. Zhou, X. Yan, Y. Chen, Y. Huang, X. Huang, E. Feng, and W. Huang, J. Phys. Chem. C **122**, 7959 (2018).

[22] J.-W. Jiang and H. S. Park, Nat. Commun. **5**, 4727 (2014).

[23] H. Wang, X. Li, J. Sun, Z. Liu, and J. Yang, 2D Mater. **4**, 045020 (2017).

[24] R. Peng, Y. Ma, Z. He, B. Huang, L. Kou, and Y. Dai, Nano Lett. **19**, 1227 (2019).

[25] L. Zhang, C. Tang, and A. Du, J. Mater. Chem. C **9**, 95 (2021).

[26] J.-H. Yuan, K.-H. Xue, J.-F. Wang, and X.-S. Miao, J. Phys. Chem. Lett. **10**, 4455 (2019).

[27] X. Bai and M. E. Kordesch, Appl. Surf. Sci. **175-176**, 499 (2001).

[28] F. Perjeru, X. Bai, and M. E. Kordesch, Appl. Phys. Lett. **80**, 995 (2002).

[29] D. Gall, I. Petrov, L. D. Madsen, J.-E. Sundgren, and J. E. Greene, J. Vac. Sci. Technol. A **16**, 2411 (1998).

[30] Y. Oshima, E. G. Víllora, and K. Shimamura, J. Appl. Phys. **115**, 153508 (2014).

[31] T. Ohgaki, I. Sakaguchi, N. Ohashi, and H. Haneda, J. Cryst. Growth **476**, 12 (2017).

[32] G. Kresse and J. Hafner, Phys. Rev. B **48**, 13115 (1993).

[33] G. Kresse and J. Furthmüller, Phys. Rev. B **54**, 11169 (1996).

[34] G. Kresse and D. Joubert, Phys. Rev. B **59**, 1758 (1999).

[35] P. E. Blöchl, Phys. Rev. B **50**, 17953 (1994).

[36] J. P. Perdew, A. Ruzsinszky, G. I. Csonka, O. A. Vydrov, G. E. Scuseria, L. A. Constantin, X. Zhou, and K. Burke, Phys. Rev. Lett. **100**, 136406 (2008).

[37] J. P. Perdew, K. Burke, and M. Ernzerhof, Phys. Rev. Lett. **77**, 3865 (1996).

[38] J. Heyd, G. E. Scuseria, and M. Ernzerhof, J. Chem. Phys. **118**, 8207 (2003).

[39] A. Togo and I. Tanaka, Scr. Mater. **108**, 1 (2015).

[40] L. Bengtsson, Phys. Rev. B **59**, 12301 (1999).

[41] Z. Ma, P. Huang, J. Li, P. Zhang, J. Zheng, W. Xiong, F. Wang, and X. Zhang, npj Comput. Mater. **8**, 51 (2022).

[42] L. Yu, Y. Wang, X. Zheng, H. Wang, Z. Qin, and G. Qin, Appl. Surf. Sci. **610**, 155478 (2023).

[43] T. P. Kaloni, Y. C. Cheng, and U. Schwingenschlögl, J. Mater. Chem. **22**, 919 (2012).

[44] L.-M. Yang, V. Bačić, I. A. Popov, A. I. Boldyrev, T. Heine, T. Frauenheim, and E. Ganz, J. Am. Chem. Soc. **137**, 2757 (2015).

[45] See Supplemental Material at http://link.aps.org/supplemental/10.1103/PhysRevMaterials.8.084407 for detailed information on structural details, tetrahedral structure, ELF diagrams, band structures, orbital-resolved band structures, Phonon spectra and AIMD simulations, Bader charge analysis, plane average electrostatic potential, and Phonon DOS calculations.

[46] Z.-J. Wu, E.-J. Zhao, H.-P. Xiang, X.-F. Hao, X.-J. Liu, and J. Meng, Phys. Rev. B **76**, 054115 (2007).

[47] E. Cadelano, P. L. Palla, S. Giordano, and L. Colombo, Phys. Rev. B **82**, 235414 (2010).

[48] C. Lee, X. Wei, J. W. Kysar, and J. Hone, Science **321**, 385 (2008).

[49] R. C. Andrew, R. E. Mapasha, A. M. Ukpong, and N. Chetty, Phys. Rev. B **85**, 125428 (2012).

[50] M. Qiao, Y. Wang, Y. Li, and Z. Chen, J. Phys. Chem. C **121**, 9627 (2017).

[51] W.-Z. Xiao, G. Xiao, Q.-Y. Rong, and L.-L. Wang, Phys. Chem. Chem. Phys. **20**, 22027 (2018).

[52] Y. Wang, F. Li, Y. Li, and Z. Chen, Nat. Commun. **7**, 11488 (2016).

[53] L. Zhou, Z. Zhou, L. Kou, A. Du, and S. Tretiak, Nano Lett. **17**, 4466 (2017).

[54] Q. Lan and C. Chen, Phys. Chem. Chem. Phys. **24**, 2203 (2022).

[55] X.-H. Hou, X.-J. Xu, J.-M. Meng, Y.-B. Ma, and Z.-C. Deng, Compos. Part B Eng. **162**, 411 (2019).

[56] M. Sanati, R. C. Albers, T. Lookman, and A. Saxena, Phys. Rev. B **84**, 014116 (2011).

[57] H. Seksaria, A. Kaur, K. Singh, and A. De Sarkar, Appl. Surf. Sci. **615**, 156306 (2023).

[58] J.-H. Yuan, G.-Q. Mao, K.-H. Xue, J. Wang, and X.-S. Miao, Nanoscale **12**, 14150 (2020).

[59] H. A. Al-Brithen, A. R. Smith, and D. Gall, Phys. Rev. B **70**, 045303 (2004).

[60] R. Deng, B. D. Ozsdolay, P. Y. Zheng, S. V. Khare, and D. Gall, Phys. Rev. B **91**, 045104 (2015).

[61] X. Z. Yan, Y. M. Chen, X. Y. Kuang, and S. K. Xiang, J. Appl. Phys. **116**, 083707 (2014).

[62] Y. Zhang and F. Liu, Appl. Phys. Lett. **99**, 241908 (2011).

[63] X. Xuan, W. Guo, and Z. Zhang, Phys. Rev. Lett. **129**, 047602 (2022).

[64] X. Xuan, M. Wu, Z. Zhang, and W. Guo, Nanoscale Horiz. **7**, 192 (2022).

[65] L. Zhang, C. Tang, C. Zhang, Y. Gu, and A. Du, J. Mater. Chem. C **9**, 3155 (2021).

[66] D. Liang, T. Jing, M. Deng, and S. Cai, Nanotechnology **32**, 155201 (2021).

[67] C. Zhang, Y. Nie, S. Sanvito, and A. Du, Nano Lett. **19**, 1366 (2019).

[68] X. Li, Q.-B. Liu, Y. Tang, W. Li, N. Ding, Z. Liu, H.-H. Fu, S. Dong, X. Li, and J. Yang, J. Am. Chem. Soc. **145**, 7869 (2023).

[69] W. Ding, J. Zhu, Z. Wang, Y. Gao, D. Xiao, Y. Gu, Z. Zhang, and W. Zhu, Nat. Commun. **8**, 14956 (2017).

[70] J. Zhao, Y. Zhao, H. He, P. Zhou, Y. Liang, and T. Frauenheim, J. Phys. Chem. Lett. **12**, 10190 (2021).

[71] M. Yagmurcukardes, Y. Qin, S. Ozen, M. Sayyad, F. M. Peeters, S. Tongay, and H. Sahin, Appl. Phys. Rev. **7**, 011311 (2020).

[72] X. Xuan, T. Yang, J. Zhou, Z. Zhang, and W. Guo, Nanoscale Adv. **4**, 1324 (2022).

[73] X. Ding, Y. Ge, Y. Jia, G. Gou, Z. Zhu, and X. C. Zeng, ACS Nano **16**, 21546 (2022).

[74] X. Ding and G. Gou, Nanoscale **13**, 19012 (2021).

[75] X. Cheng, S. Xu, F. Jia, G. Zhao, M. Hu, W. Wu, and W. Ren, Phys. Rev. B **104**, 104417 (2021).

[76] Z. Liu, J. Pan, Y.-F. Zhang, and S. Du, J. Phys.: Condens. Matter **33**, 144002 (2021).

[77] X. Liu, L. Li, C. Yang, C. Bai, and J. Li, J. Mater. Chem. A **11**, 21735 (2023).

[78] M. Wu and X. C. Zeng, Nano Lett. **16**, 3236 (2016).

[79] S.-H. Zhang and B.-G. Liu, Nanoscale **10**, 5990 (2018).

[80] X. Xie, M. Chen, M. Yu, J. Li, M. Zhao, and L. Li, Results Phys. **53**, 106988 (2023).